Frequency-tunable Transmon qubit in a 3D copper cavity

Johannes Fankhauser, *fankhauj@student.ethz.ch*

Semester thesis, Physics department
ETH Zürich

Supervisors: Philipp Kurpiers, Andreas Wallraff

August 12, 2016

Abstract

Superconducting qubits are promising physical realizations of quantum bits (qubits). These qubits are made of superconducting circuits including elements such as capacitors, inductors and Josephson junctions. Here we design and measure a frequency-tunable Transmon qubit operated in a 3D copper cavity where the transition frequency of the Transmon can be tuned via an external coil mounted to the cavity. The use of a 3D cavity should also allow a better protection of the qubit from decoherence sources and the use in further experiments. In the experimental tests an internal quality factor of $Q \approx 16000$ of the cavity at 10 mK and an energy relaxation time $T_1 \approx 15$ µs are achieved. Furthermore, the qubit is shown to be tunable in frequency by approximately a full period through the external coil.

Contents

1 Introduction

The interaction strength between a microwave photon and superconducting qubit has proved to be a few thousand times that of the well-known atom-photon interaction [3]. The so-called strong coupling condition can be rather easily achieved in the superconducting circuit. Therefore, new parameter regions that are difficult to achieve with the ordinary atom/molecule cavity QED can be opened up by the cavity-QED in Josephson circuits. The Josephson junctions also allows itself to be tunable by external B-fields through so called Superconducting Quantum Interference Devices (SQUID) which are designed to couple to flux of external fields. This freedom in parameter control makes it very attractive for the use in quantum devices. In this experiment we use a 3D microwave cavity for coupling and interaction with superconducting qubits where we incorporate a coil into the cavity to control the qubit's transition frequency. The cavity is fabricated of copper to make it transparent to the magnetic field of the tuning coil. On the other hand, such cavities experience a lower quality factors than microwave cavities made out of superconducting metals.

2 Some Quantum Information Theory

2.1 Quantum bit

The quantum mechanical counterpart of the classical bit is called the quantum bit or *qubit*. As the classical bit has two states 0 and 1 the qubit can be measured to be in one of the two states $|0\rangle$ and $|1\rangle$. In the general description of quantum mechanics, however, the state of the qubit can be in superposition of its basis states

$$|\psi\rangle = c_1|0\rangle + c_2|1\rangle, \tag{2.1}$$

where c_1, $c_2 \in \mathbb{C}$ are normalized through $|c_1|^2 + |c_2|^2 = 1$. According to the measurement postulate the state $|\psi\rangle$ is projected to one of the basis states $|0\rangle$ or $|1\rangle$ with probability $|c_1|^2$ and $|c_2|^2$, respectively.

3 Implementation of the qubit

Any quantized harmonic oscillator has discrete energy levels with equal sized energy gaps between them. However, this condition is not sufficient to address a specified pair of levels and drive a transition between only two levels of choice which ought to act as qubit states. All the levels can be excited by irradiating resonant microwaves. To overcome this issue, we can introduce some anharmonicity in the potential of the oscillator by adding the non-linear Josephson element which leads to energy levels not equally spaced [1].

3.1 Transmon qubit

For instance, if we make an LC-circuit with superconducting material, the quantum energy levels in the superconducting gap will be available to realize a quantum bit. However, since the LC-circuit is equivalent to a harmonic oscillator, every energy level spacing has the same value. Adding a Josephson junction to the circuit to make it a so called Transmon qubit will introduce the desired anharmonicity. Essentially, the Transmon qubit is a solid state electrical circuit with superconducting elements [1]. The basic feature which introduces non-linearity is the Josephson junction, a non-dissipative circuit element.

3.1.1 The Josephson junction

As illustrated in figure 1, a Josephson element consists of two thin superconducting films with an insulating oxide layer separating them. At cryogenic temperatures the Josephson tunnel junction behaves as a non-linear inductor in parallel with a capacitance corresponding to the two overlapping electrodes of the junction. This model can be analyzed be quantizing the classical version from conventional circuit theory [1]. Since ordinary magnetic flux is only defined for closed loop, we introduce the branch flux of an electric element

$$\Phi(t) := \int_{-\infty}^{t} V(t')dt', \tag{3.1}$$

with $V(t)$ the path integral of the electric field along a current line inside the element. For the Josephson junction we obtain a non-linear behavior in the flux-current dependence as the current reads as

$$I(t) = I_0 \sin\left(\frac{2\pi\Phi(t)}{\Phi_0}\right), \tag{3.2}$$

where $\Phi = \frac{h}{2e}$ the flux quantum. This is unlike the linear relationship in a conventional conductor where $I(t) = \frac{\Phi(t)}{L}$. It is often common to define a new variable $\theta := \frac{2\pi\Phi(t)}{\Phi_0} \mod 2\pi$ which is the phase difference between the two superconducting condensates on both sides of the junction when discussing the superconducting ground state. One of the parameters which the Josephson element is generally described with is the Josephson energy $E_J := \varphi_0 I_0$, $\varphi_0 := \frac{\Phi_0}{2\pi}$. Thus for the energy stored in the junction we find

$$\begin{aligned} E(t) = \int_{-\infty}^{t} V(t')I(t')dt' = \int_{-\infty}^{t} \frac{d\Phi(t')}{dt'} I_0 \sin\left(\frac{2\pi\Phi(t')}{\Phi_0}\right) dt' \\ = -E_J \cos\left(\frac{2\pi\Phi(t)}{\Phi_0}\right), \end{aligned} \tag{3.3}$$

where we substituted 3.1 and 3.2. Note that it is assumed that initially for the circuit $V(-\infty) = \phi(-\infty) = 0$. Another important characteristic parameter is the Coulomb charging energy

$$E_{C_J} := \frac{(2e)^2}{2C_J} \tag{3.4}$$

with C_J the junction capacitance.

3.1.2 SQUID loop

Our Transmon qubit contains a Superconducting Quantum Interference Device (SQUID) whose Hamiltonian reads

$$H = \frac{q^2}{2(C_J + C)} - E_J \cos\left(\frac{2e}{\hbar}(\Phi - \Phi_{\text{ext}})\right), \tag{3.5}$$

where E_J is the total Josephson energy of the two junctions in parallel. We quantize the Hamiltonian by introducing the charge number $n := q/2e$ and using the phase difference ϑ described in 3.1.1. Analogously to the variables of the harmonic oscillator the new parameters n and ϑ are considered to fulfill the commutation relation $[n, \vartheta] = i$, where n has integer values and $\vartheta \in [0, 2\pi]$. Additionally, we define $E_C := \frac{(2e)^2}{2(C_J+C)}$ and find

$$H = E_C(n - Q_r/(2e))^2 + E_J \cos\left(\vartheta - \frac{2\pi\phi_{\text{ext}}}{\phi_0}\right). \tag{3.6}$$

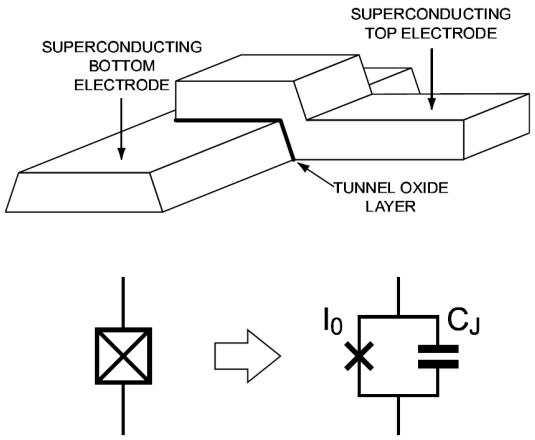

Figure 1: The Josephson junction consists of two superconducting electrodes separated by a thin tunnel oxide layer. In circuit diagrams we use the irreducible circuit element [1].

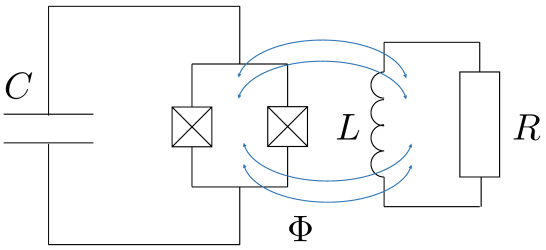

Figure 2: A Transmon qubit consisting of a SQUID with a shunt capacitance C acting as an antenna and simultaneously reducing the charge noise on the junction. The external coil L controls the magnetic flux through the loop. The tunnel junctions in parallel result in an effective Josephson energy E_J.

The ϕ_{ext} will be the external flux applied on the SQUID from the tuning coil. Note that we have artificial introduced Q_r which is the residual offset charge on the capacitor and can not be eliminated with a canonical transformation as in a harmonic circuit due to the non-linearity of the tunnel junction. The energy values E_C and E_J will be the characterizing parameters in our measurements of the Transmon qubit [4].

3.1.3 Tuneability through a coil

We achieve tunability of the qubit transition frequency by using an external coil inserted in the outer shell of the cavity. The procedure is called flux tuning since the static magnetic field alters the magnetic flux through the SQUID loop and consequently its transition frequency. Figure 3 shows a sketch of the setup.

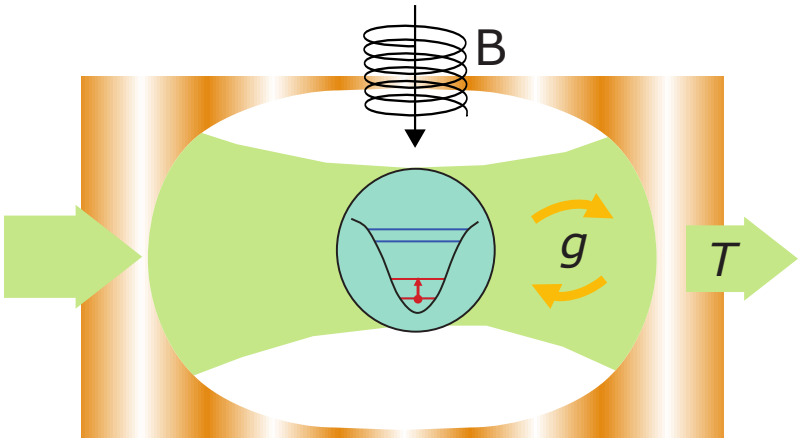

Figure 3: 3D cavity with external coil. The static magnetic field of the coil alters the Hamiltonian of the qubit inside the coil and therefore shifts the transition frequency. Green areas indicate the microwave field which couples to the qubit. Part of the incoming microwaves are transmitted through the cavity depended on the state of the qubit.

3.2 Resonator

In circuit quantum electrodynamics, resonators for microwave frequencies mainly suppress spontaneous emission, protect superconducting qubits from decoherence and are used for readout [5]. Transmon quibits can be controlled and read out with different kinds of resonators. Here we use a 3D copper cavity. The cavity limits the microwaves inside to certain modes with widths depending on the material and manufacturing quality of the cavity and couples the electromagnetic modes to the superconducting qubit states.

3.2.1 Quality factors

In the context of resonators the quality factor is defined by

$$Q := \frac{f_0}{\Delta f}, \tag{3.7}$$

where f_0 is the resonant frequency of the cavity and Δf is the half-power bandwidth, i.e. the bandwidth over which the power of vibration is greater than half the power at the resonant frequency [5].

3.2.2 Purcell Effect

The reason why the qubit is put inside a cavity is that the spontanous emmision of a quantum system and hence the decoherence is significantly surpressed when the modes it can radiate into are limited. Thus, in an ideal experiment the best would be to have one infinitely sharp mode such that the qubit never decays when it is detuned from this frequency. However, since the qubit is at the same time driven with the external microwave field, a certain width of the resonance is necessary to drive the qubit at the first place. The magnitude of enhancement of spontaneous emission rates when they are matched in a resonant cavity is given by the Purcell rate

$$\Gamma_P^{01} = \frac{g^2}{\Delta^2}\kappa, \tag{3.8}$$

where g is the coupling to the cavity, Δ the detuning of qubit frequency and resonator and κ double the rate with which the resonator relaxes the qubit in the limit of zero detuning.

Note that κ is inversely proportional to the quality factor of the cavity described in 3.2.1. From here we see the dependence of the decaying rate on the quality factor [6].

3.3 3D cavity resonator

3.3.1 Electromagnetic modes

We consider a rectangular cavity with conducting walls and derive the electromagnetic TE and TM eigenmodes and frequencies in the cavity. Energy is stored within the cavity and also dissipated in the conducting walls. We assume vacuum inside the cavity. A common approach to find solutions for the modes in a cavity is to first solve the problem for a rectangular waveguide and then terminate both sides to find the cavity modes. The procedure is described in appendix D.

4 Coupling the qubit to the cavity

Cavity quantum electrodynamics (cavity QED) describes the interaction between a qubit and light inside a cavity. Systems in a cavity interact almost exclusively with the resonant modes of the cavity, i.e. with photons of well-defined frequencies.

4.1 Jaynes Cummings Hamiltonian

The Hamiltonian of a light mode with frequency ω_0 can be described as a harmonic oscillator, that is

$$H_{EM} = \hbar\omega_0 a^\dagger a, \tag{4.1}$$

where we omit the vacuum energy. Even though the cavity might have more than one resonant mode, we suppose that the other modes are far detuned from the transition frequency of the qubit. Assuming that the qubit can be modeled as a two-level system the Hamiltonian reads

$$H_Q = \frac{1}{2}\hbar\omega\sigma_z, \tag{4.2}$$

where ω is the transition frequency of the qubit and σ_z the Pauli-Z matrix. The full Hamiltonian of the system then yields

$$H = \frac{1}{2}\hbar\omega(B)\sigma_z + \hbar\omega_0 a^\dagger a + \hbar g(\sigma_+ a + \sigma_- a^\dagger) \tag{4.3}$$

and is called the Jaynes-Cummings Hamiltonian (JC Hamiltonian). The transition frequency ω depends on the strength of the external field B. The JC Hamiltonian holds under the rotating wave approximation with $|\Delta| := |\omega_0 - \omega| \ll \omega_0 + \omega$. The parameter g is the coupling strength between cavity and qubit. The eigenstates of the Hamiltonian are the so-called dressed states [4].

$$|n, +\rangle = \sin(\vartheta/2)\,|n+1, 0\rangle + \cos(\vartheta/2)\,|n, 1\rangle \tag{4.4}$$

$$|n, -\rangle = \cos(\vartheta/2)\,|n+1, 0\rangle - \sin(\vartheta/2)\,|n, 1\rangle, \tag{4.5}$$

which are superpositions of the photon number n and the ground and excited states $|0\rangle$, $|1\rangle$ of the qubit. The angle ϑ is defined over $\tan(\vartheta) = -\frac{2g\sqrt{n+1}}{\Delta}$. The eigenenergies of these states are

$$E_\pm = \omega_0\left(n + \frac{1}{2}\right) \pm \frac{\Delta}{2}\sqrt{1 + \frac{4g^2(n+1)}{\Delta^2}} \tag{4.6}$$

4.2 Read out and frequency shift

For large detuning Δ the energies tend to the uncoupled values

$$E_{\pm} \to \omega_0 \left(n + \frac{1}{2}\right) \pm \frac{\Delta}{2} = \begin{cases} \omega_0(n+1) - \frac{\omega}{2} \\ \omega_0 n + \frac{\omega}{2} \end{cases} , \tag{4.7}$$

which we call the dispersive regime and the coupling can be treated as a perturbation. If we expand the coupled eigenenergies for $g \ll \Delta$ the energies give

$$E_{\pm} = \begin{cases} \left(\omega_0 + \frac{g^2}{\Delta}\right)(n+1) - \frac{\omega}{2} \\ \left(\omega_0 - \frac{g^2}{\Delta}\right) n + \frac{\omega}{2} \end{cases} . \tag{4.8}$$

From this we see that the cavity frequency undergoes a shift, whose sign depends on the state of the qubit. This so called dispersive shift is used to read out the qubit state by measuring the cavity's resonant frequency. We can summarize the frequency shift of the qubit in the effective Hamiltonian of the whole system

$$H \approx \hbar \left(\omega_0 + \frac{g^2}{\Delta}\sigma_z\right) a^{\dagger}a + \frac{\hbar}{2}\left(\omega + \frac{g^2}{\Delta}\right)\sigma_z, \tag{4.9}$$

where the cavity undergoes a frequency shift depended on the state of the quibit as well as the qubit frequency itself [4].

5 Simulation

This section contains the analysis of the electromagnetic modes and their external quality factors in the cavity, the strength of the B-field where the qubit is placed and the shunted capacitance of the squid loop when inside the copper cavity. The analysis is done in COMSOL Multiphysics 5.0 [8] except for the latter.

5.1 Cavity modes and Ports

As described in chapter 3.3.1 we expect distinct electromagnetic modes in the cavity. For manufacturing we model the boundary as a rectangular shape but with rounded edges of radius $\frac{w}{2}$ to avoid peak effects at sharp corners, where w is the width of the cavity. This leaves us with three parameters l, w, h (length, width and height) for the geometry of our cavity. Those degrees of freedom are used to adjust the frequency of the first mode TE_{101} to be at 7 GHz in order to measure the tuned qubit with maximum transition frequency of 8.5 GHz above and below the cavity mode. An additional degree of freedom is given by the position of the ports, i.e. where we place the input and output pins to drive and read out the cavity. The ports are placed at the nodes of the mode at 10.5 GHz which would also drive the qubit. In figure 4 results from the simulation of the first three modes are shown. The final dimensions of the cavity are $l = 50$ mm, $w = 22.64$ mm and $h = 5$ mm. The length of the port pins which stick into the cavity mainly determine the quality factor of the modes. The simulation assumes vacuum and a conductivity of the OFHC copper of $\sigma = 10^9$ S/m reflects the conditions in the cryostat.

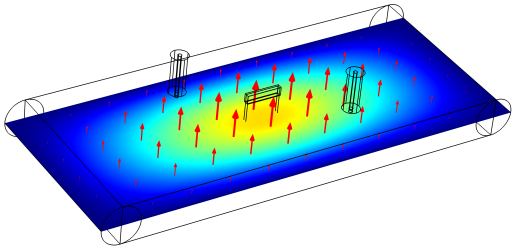

(a) The ground mode of the cavity with frequency of $f_{101} \approx 7$ GHz.

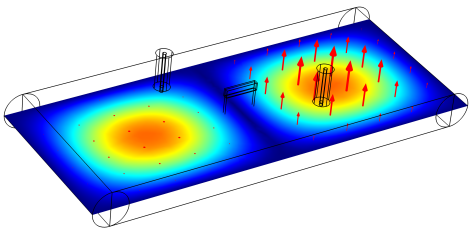

(b) The first higher mode of the cavity at $f_{102} \approx 8.6$ GHz.

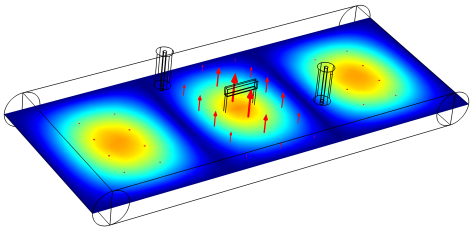

(c) The second higher mode of the cavity at $f_{103} \approx 10.5$ GHz.

Figure 4: The TE_{101}, TE_{102} and TE_{103} modes of the cavity obtained from the simulation. The picture shows a wireframe of the inside volume of the cavity. The ports are placed at the nodes of the TE_{102} mode which would couple to the qubit too. The field strength is encoded by colored areas which show the maximum absolute value of the electromagnetic field. Red arrows denote E-field vectors. In the center of the cavity the sapphire chip is shown on which the qubit is located.

Due to symmetry of the port sites, in the simulation the pin lengths were chosen to have the same length since the quality factors of the individual input and output ports equally add up to the overall external quality factor $\frac{1}{Q_{\text{ext}}} = \frac{1}{Q_{\text{Port}_1}} + \frac{1}{Q_{\text{Port}_2}}$. The length is then designed to reach an external quality factor of $Q_{\text{ext}} \approx 8200$. Additionally, we can then control the individual lengths of the pins to achieve the desired individual quality factors. In figure 5 the quality factor of all the modes up to 14 GHz are shown at the final pin length of $l_1 = 4$ mm for the input port and $l_2 = 4.6$ mm for the output port. The quality factor of the TE_{103} mode at $f_{103} \approx 10.5$ GHz shows a high quality factor of $Q_{\text{ext}} \approx 7 \cdot 10^7$ due to the placement of the ports at the nodes of this mode and the resulting weak coupling.

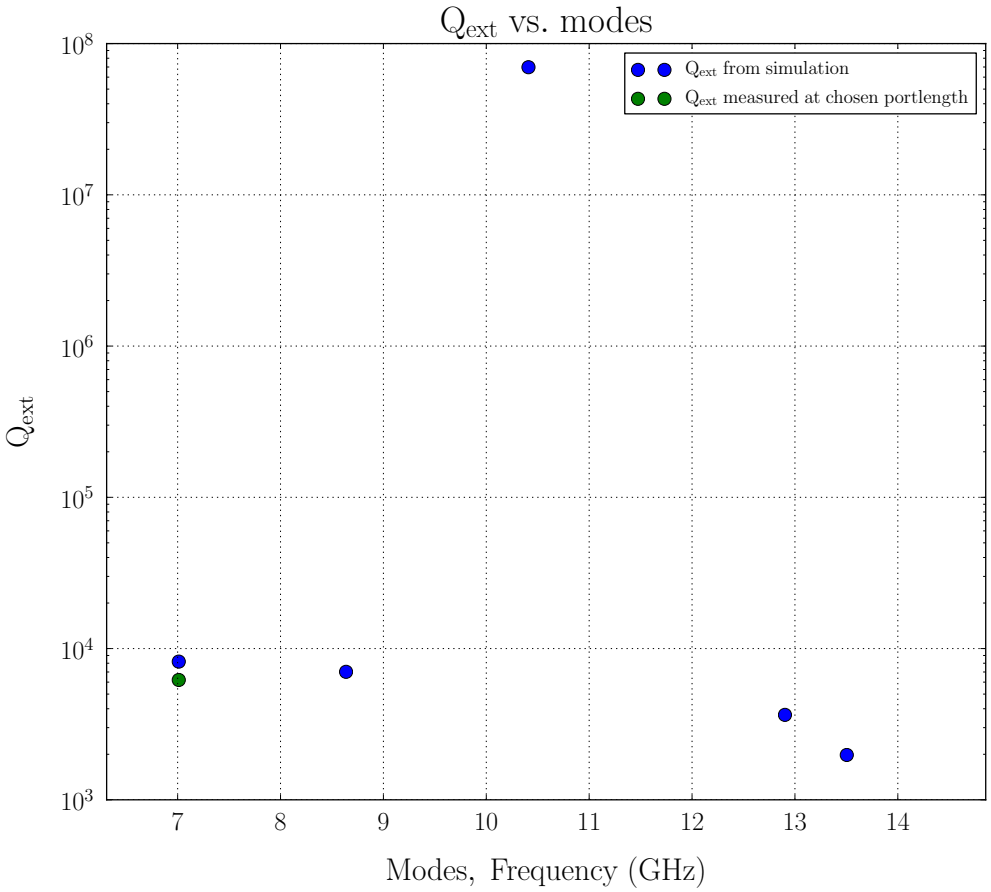

Figure 5: External quality factors of all cavity modes up to 14 GHz. The blue data-points come from the simulation, whereas the green data-point depicts the measured external quality factor of the OFHC copper cavity.

5.2 B-field of coil and tunability

The B-field of the external coil mounted in the copper cavity should be strong enough at the position of the qubit to produce the necessary flux in the SQUID loop to tune the qubit frequency at least over one period. The loop size of the SQUID is designed to be 7×7 µm, large enough to drive the qubits frequency over a whole period. We simulate the coil and probe the B-field at the qubit's position as a function of the applied current in the coil. The coil used in the simulation has 1500 windings with a test current of 0.5 A and an inner radius of $r = 2.25$ mm. The optimal coil radius for the B-field to be strongest at the qubit site is approximately 11.1 mm. For this to obtain, we use the exact formula for the B-field on the symmetry axis of a coil with radius r

$$|\vec{B}(r,h)| = \frac{N\mu_0 I}{2}\frac{r}{r^2+h^2} \tag{5.1}$$

and locate the maximum as shown in 6. Where $N = 1500$ is the number of windings and $h = 11.32$ mm is the distance of the Transmon to the center of the coil. However, we want to use the small coil with $r = 2.25$ mm as this is the standard one used for our experiments. Figure 7 is a visualization of the magnetic field of the coil and in figure 8 the transition frequency of the qubit versus the applied current is plotted.

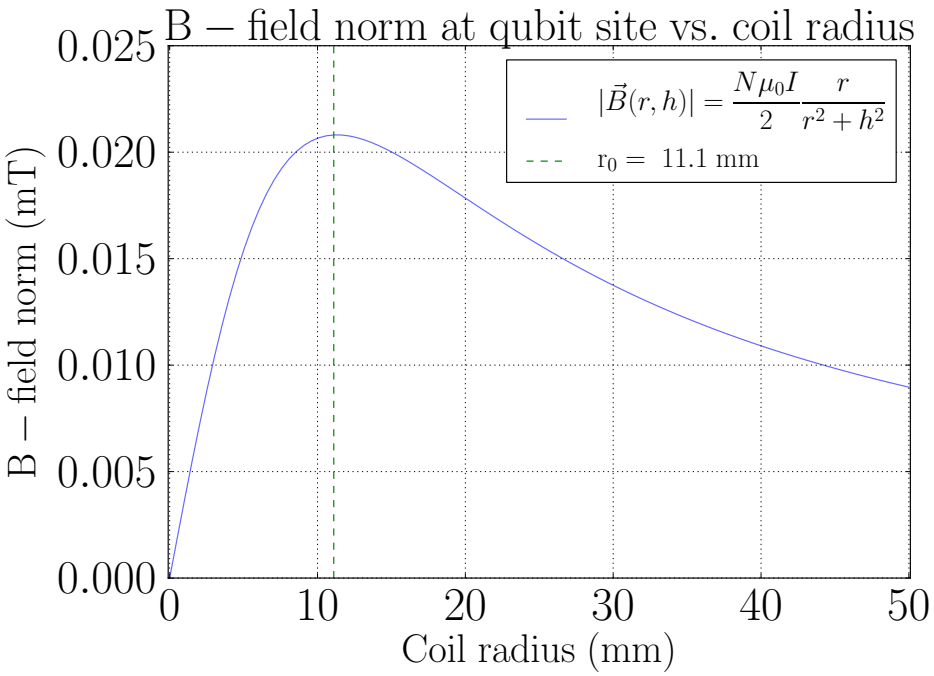

Figure 6: The B-field norm of the external coil probed at the qubit site as a function of the coil radius. A radius of $r_0 \approx 11.1$ mm yields the maximum B-field strength.

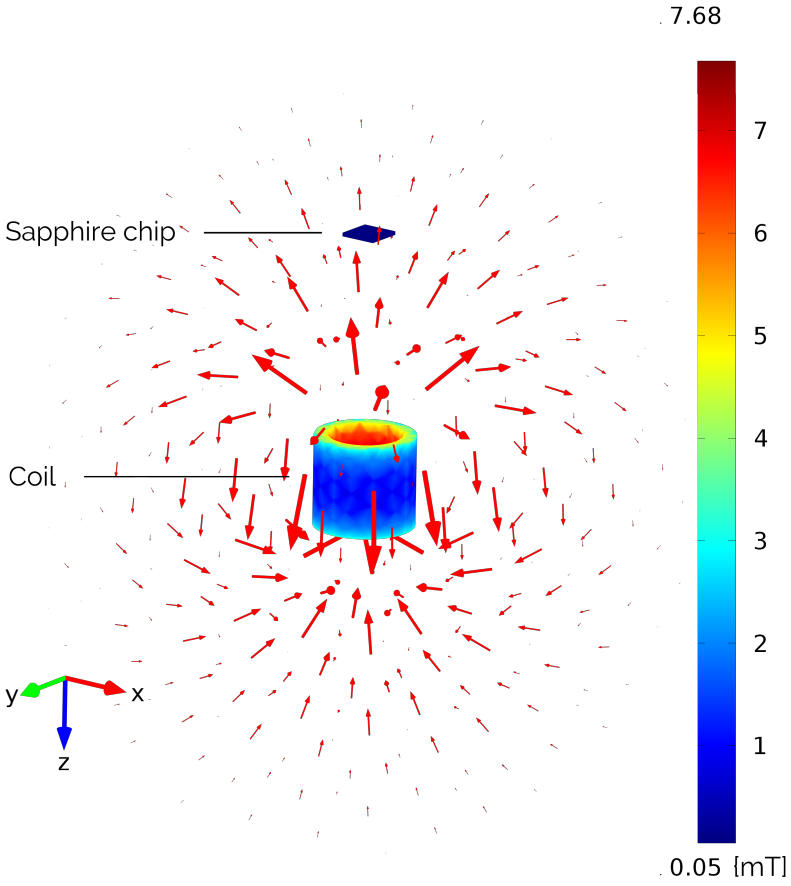

Figure 7: The simulated B-field of the external coil probed at the qubit position. Red arrows indicate the B-field vectors and colors on the coil and chip the B-field norm.

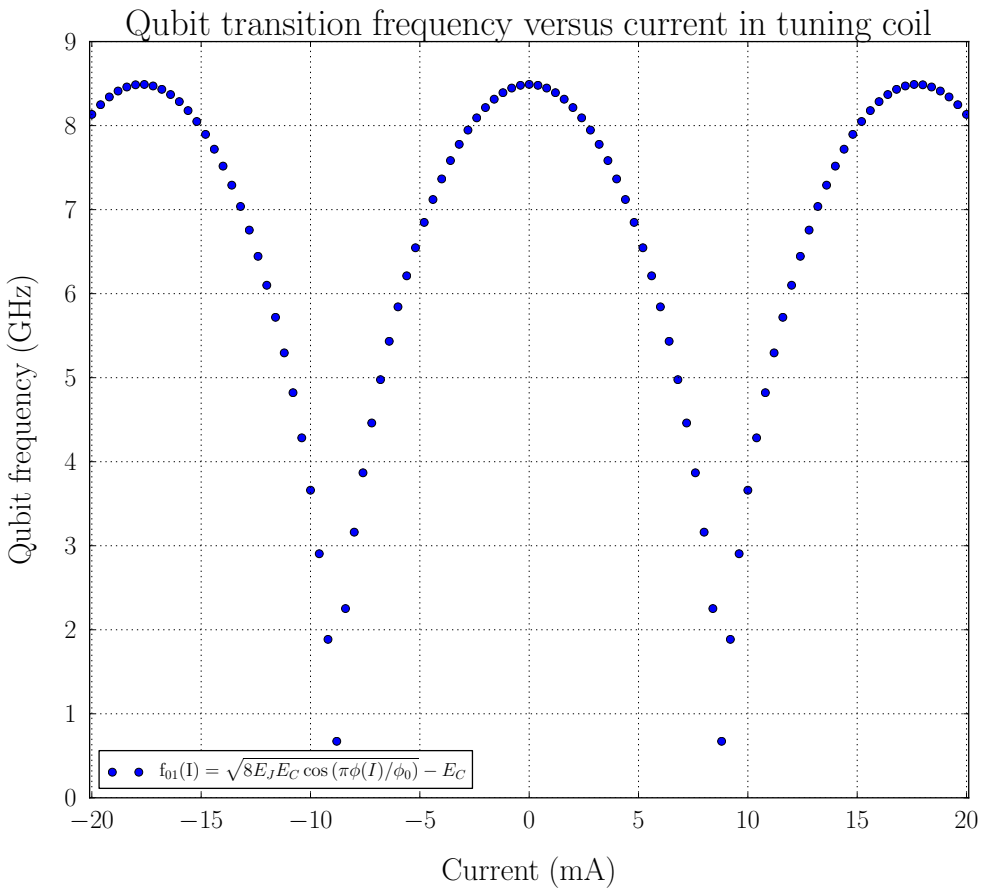

Figure 8: The simulated transition frequency of the qubit versus the applied current in the external coil.

5.3 Shunted capacitance

The two aluminum pads which are connected to the SQUID form the capacitor of the Transmon qubit as shown in figure 2. A simulation in ANSYS Maxwell 15.0 [9] is used to calculate the capacitance matrix of the two pads and the wall of the cavity. The design parameters of the pads are length a, width b and the spacing c between them (see figure 9 for details). The parameters are optimized to achieve a Coulomb charging energy $E_C/h = 300$ MHz and a coupling strength $g/(2\pi) = 100$ MHz, where h is the Planck constant. These are values of a regular Transmon qubit. Figure 9 shows the final design under the microscope. The dimensions used for the final design are $a = 400$ µm, $b = 440$ µm and $c = 200$ µm.

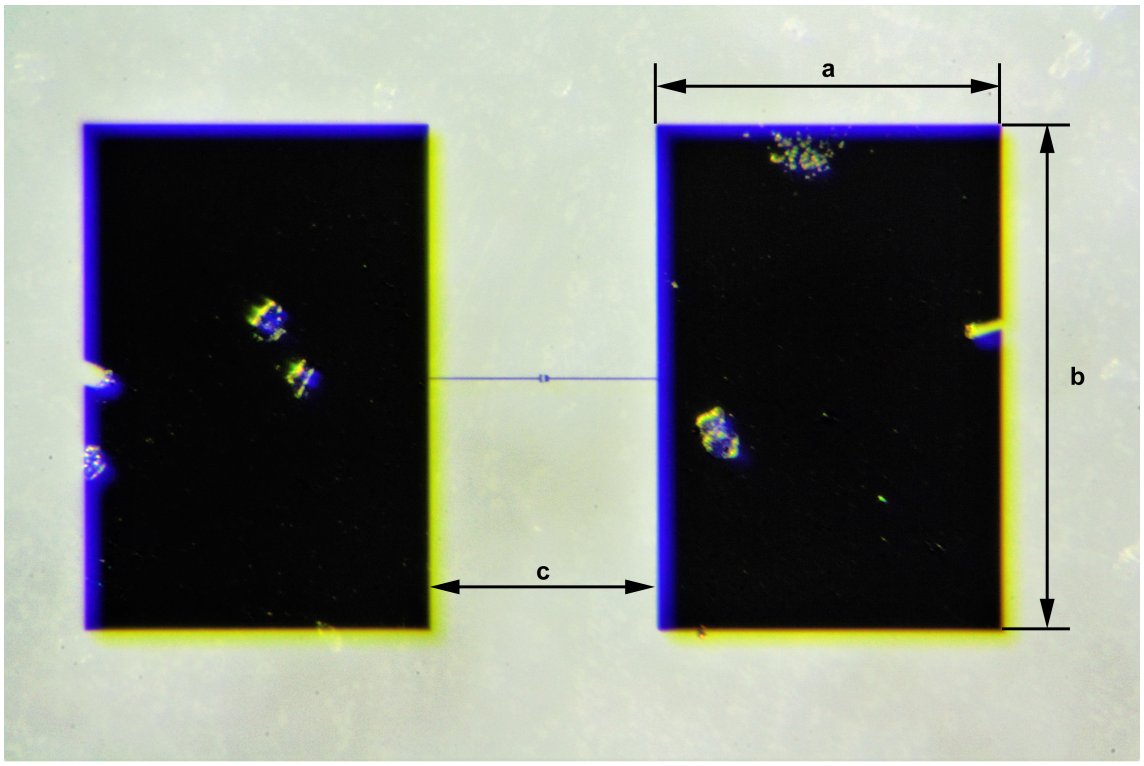

Figure 9: The Transmon qubit under the microscope. The capacitive aluminum pads which couple to the cavity modes are connected to the SQUID in the center line between the pads.

6 Experimental setup

6.1 3D Transmon

In addition to the designed parameters mentioned in chapter 5.3 the maximum qubit frequency was designed to be at $f_{ge}^{max} = 8.5$ GHz. This frequency corresponds to a Josephson energy $E_J/h = 32.2$ GHz. However, for the tests in the dilution refrigerator a Transmon qubit with an $E_J/h = 24$ GHz, i.e. $f_{ge}^{max} = 7.2$ GHz was fabricated. The Transmon is fabricated on a sapphire chip which is held in place by a tight fit of the cavity.

6.2 Copper Cavity

The cavity in our study is machined from bulk oxygen-free high-conductivity copper (OFHC copper) to reduce losses. The insides of the cavity are finished by milling without further polishing or honing followed by subsequent treatment of both cavity parts with citric acid for about 30 minutes. The cavity is blown dry with nitrogen gas. The 3D cavity is coupled by an exposed center pin to a coaxial cable. The pins portruding into the cavity are depicted in figure 12a. For the measurements at room temperature and 4 K the used pin length is chosen to not reach into the mode volume of the cavity in order for the contribution of the external quality factor to be negligible. Hence, the internal quality factor of the cavity is measured. This can be seen in the relationship between the quality factors

$$\frac{1}{Q} = \frac{1}{Q_{\text{int}}} + \frac{1}{Q_{\text{ext}}}, \tag{6.1}$$

with Q the quality factor of the cavity, Q_{int} its internal quality factor and Q_{ext} the external quality factor due to losses other than the losses in the cavity. The closed cavity with

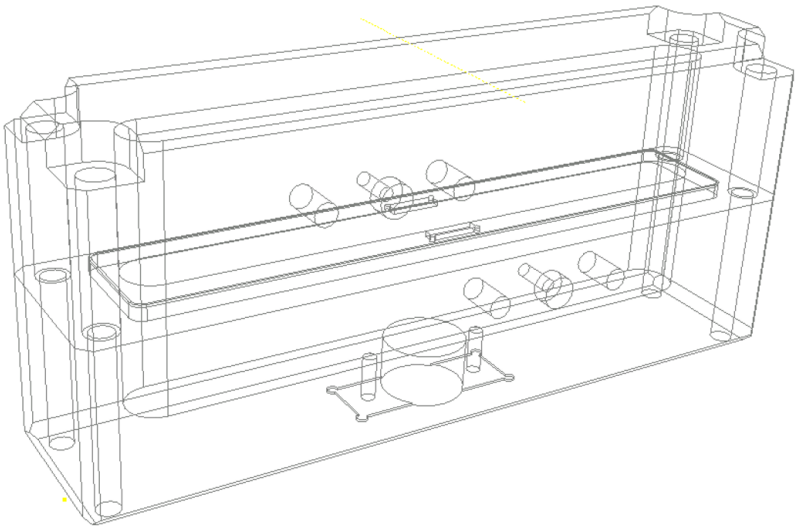

Figure 10: A wireframe sketch of the copper cavity designed in Autodesk Inventor [10]. On the lower part the coil is mounted into the cylindrical shaped inner space. The input and output ports are installed by screws at the threads.

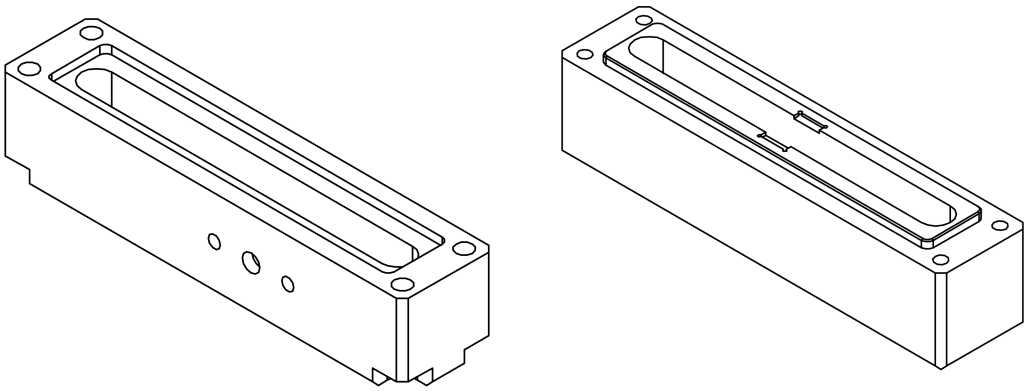

(a) Top part of the designed copper cavity.

(b) Bottom part of the designed copper cavity.

Figure 11: The two parts of the copper cavity. The groove ensures an accurate alignment.

mounted coupler is shown in 12b. The modeling of the cavity is done in Autodesk Inventor. A wireframe model of the cavity and the two parts of it are depicted in figures 10 and 11.

6.3 Cabling setup

For measurements in the dilution refrigerator microwave signals generated by the microwave generator (MWG) pass through three 20 dB attenuators on the 4 K, 100 mK and base temperature (BT) stages and reaches the cavity with the qubit. One of the ports of the SMA connector is connected to two isolators at 20 mK, a bandpass for $4-8$ GHz, an isolator at 100 mK, and a High-Electron-Mobility-Transistor (HEMT) amplifier at the 4 K- stage for $4-8$ GHz followed by room temperature amplification and downconversion to 250 MHz. The signal is digitized by an analog-digital-converter (ADC) on a field-programmable-gate-array (FPGA). Figure 13a shows the schematic of the measurement setup in the cryostat.

For the measurements at room temperature and 4 K the cavity is directly connected to

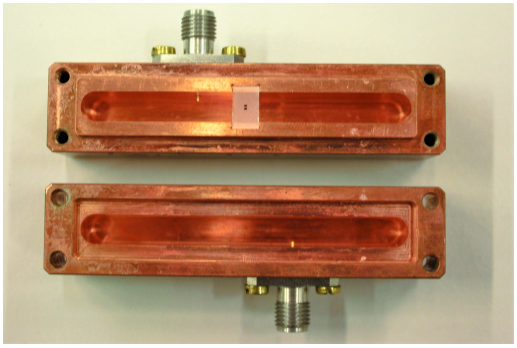

(a) The two parts of the cavity. One can see the mode volume, the sapphire chip where the qubit is attached and the pins of the ports extending into the mode volume.

(b) Front view of the copper cavity with connectors.

Figure 12: The fabricated cavity, opened and closed.

the vector network analyzer (VNA) via two calibrated coaxial cable. Figure 13b depicts the measurement scheme at room temperature.

S - parameter: In the s-parameter approach, an electrical network is treated as a 'black box' containing various interconnected electrical circuit components or lumped elements such as resistors, capacitors, inductors and transistors, which interact with other circuits through ports. The network is characterized by a square matrix of complex numbers called S-parameter matrix, which can be used to calculate response to signals applied to the ports. In the experiments we measure the transmission of the cavity to determine its properties. That is, the parameter S_{21} which is the ratio of transmitted and incident power wave [7].

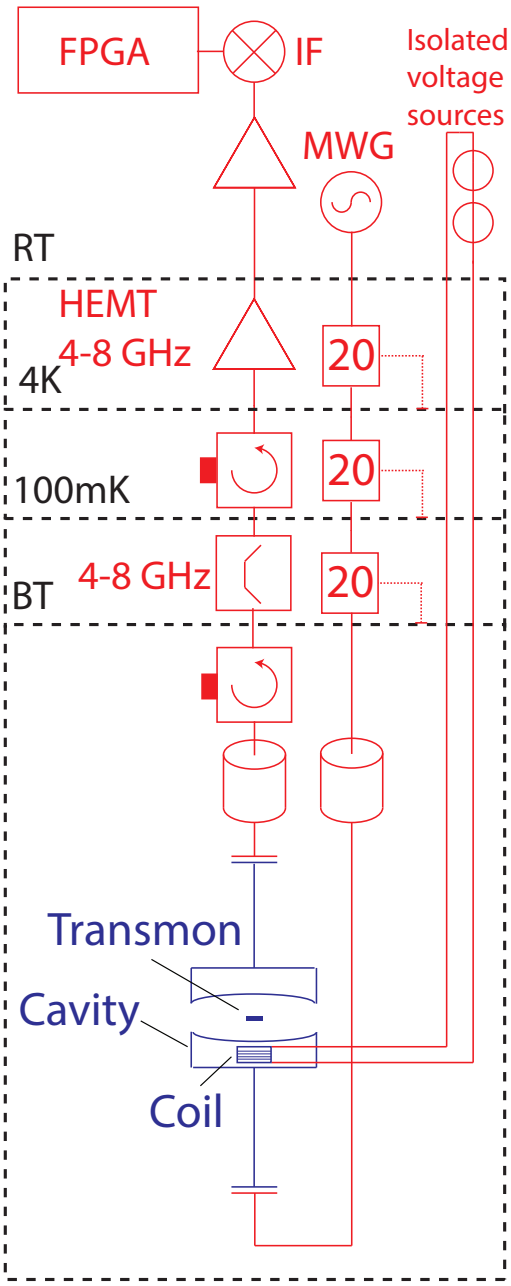

(a) Measurement setup in cryostat. The microwave signal passes through several attenuators and reaches the cavity. After that, the signal passes through an isolator, a bandpass, another isolator, a HEMT and eventually reaches the mixer and FPGA.

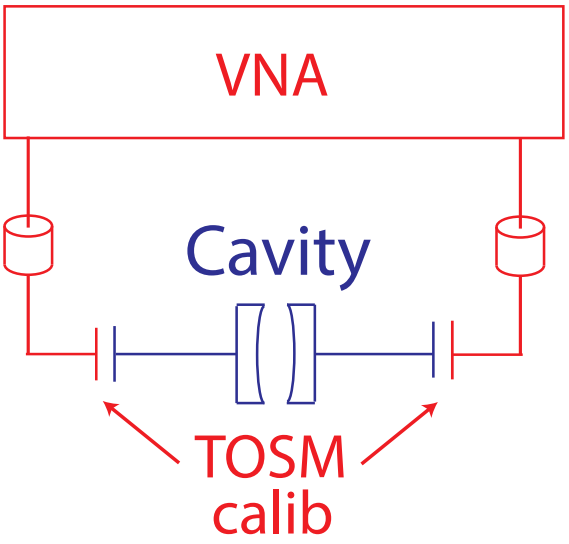

(b) Measurement setup at room temperature and 4 K. The cavity is directly connected to the virtual network analyzer (VNA) via calibrated coaxial cables.

Figure 13: Measurement setups in cryostat and at room temperature.

7 Experimental Results

7.1 Q factor and pin length

Figure 14a shows the external quality factor of the cavity versus the pin length. The longer the pins of the ports the further they reach into the mode volume and increase coupling. Therefore, the quality factor decreases for larger pin lengths. Since the internal quality factor is an intrinsic property of the cavity and accounts only for damping losses in the boundary of the mode volume, Q_{int} stays nearly independent of the pin length as shown in figure 14b. Figure 14c as well fits the expectation which equation 6.1 suggests as the quality factor tends to a constant value for short port lengths.

7.2 Q factor and temperature

We measure the s_{21} parameter on the VNA to obtain the dependence of the quality factor of the copper cavity on the temperature. We collect data at room temperature $T = 293$ K, at $T = 4$ K with a dipstick measurement in liquid Helium and at $T \approx 10$ mK at the base temperature stage of the dilution refrigerator. As shown in figure 15a, 15b and 15c the quality factor increases with decreasing temperature which is expected due to the increasing conductivity of copper. For the quality factors to be determined we fit the measurements to a Lorentzian peak which accounts for measurement errors due to a constant noise offset and linear dependence:

$$|S_{21}(f)| = a + b \cdot f + c\frac{1}{1 + 4\left(\frac{f-f_0}{\kappa}\right)}, \tag{7.1}$$

where f_0 is the resonant frequency and κ the width. The error bars shown in the plots come from averaging the noise far detuned from the peak. The measurement at cryogenic temperatures uses the pin lengths of 3.75 mm in order to be able to couple to the cavity mode at very low power as the external quality factor at 3.75 will be lower compared to the measurements at higher temperature as shown in 14c. Neither the cryostat nor the dipstick measurement at liquid Helium temperature allow to calibrate the whole connector line to the cavity, thus, the internal quality factor is greater. If we assume the external quality factors to be the same at room temperature and base temperature $Q_{\text{ext}}(RT) = Q_{\text{ext}}(BT)$, we can estimate the internal quality factor Q_{int} since the external quality factor at room temperature was measured:

$$Q_{\text{int}} \approx \frac{1}{\frac{1}{Q} - \frac{1}{Q_{\text{ext}}(RT)}} \approx 16120 \tag{7.2}$$

at base temperature.

7.3 Tuned qubit frequency

From the analysis of the simulation of tunability in chapter 5.2 we expect a B-field dependence as shown in figure 8. Note that the for the simulation a maximum qubit frequency of $f_0 = 8.5$ GHz was assumed. For the experiment, however, a qubit with only $f_0 = 7.2$ GHz was availably. Accordingly, the maxima of the tuning curve should be at this frequency. In the regime where the detuning Δ tends to zero the quantum system takes on the dressed states and we see avoided level crossing when qubit frequency and cavity frequency start to match. Hence, the measurement reveals two peaks at each frequency each corresponding to the hybrid system. Only when the detuning Δ is sufficiently large, the approximation of the uncoupled states applies and one can uniquely identify the qubit and cavity frequency peak. Figure 16 shows the resonator spectroscopy and is well in agreement of

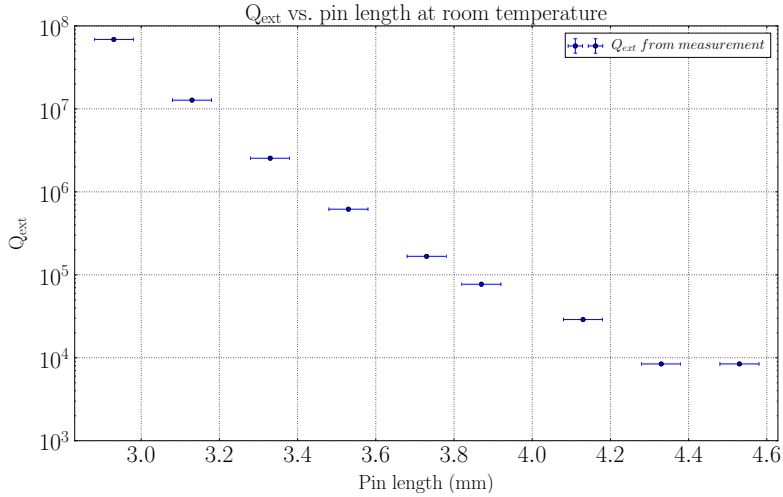

(a) The external quality factor of the cavity versus the length of the port pins at room temperature.

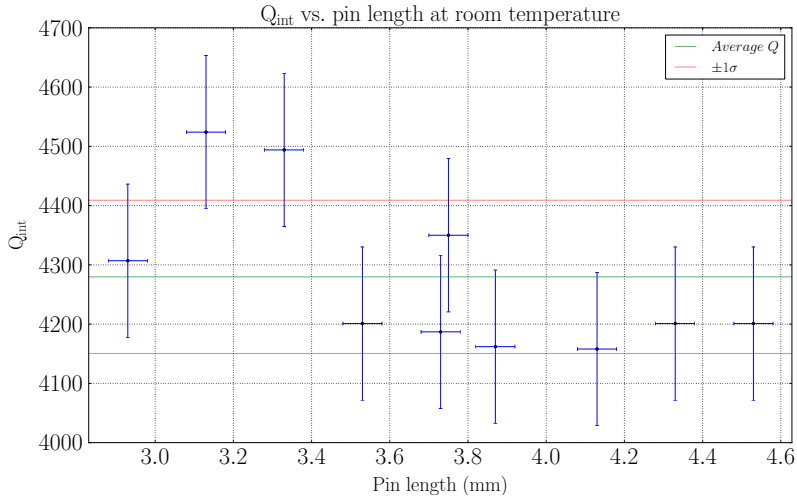

(b) The internal quality factor is nearly independent of the length of the pins. The measurement is done at room temperature. The mean noise where the Lorentz peak levels off is used for the errors in Q_{int}.

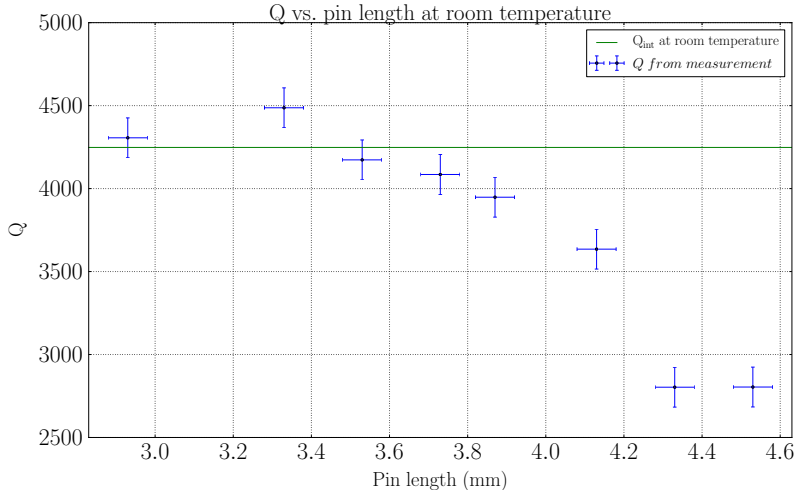

(c) The loaded quality factor of the cavity for different lengths of the port pins at room temperature. For short pins the quality factor tends to the internal quality factor of the cavity.

Figure 14: Measurements of the quality factors versus the pin length at room temperature.

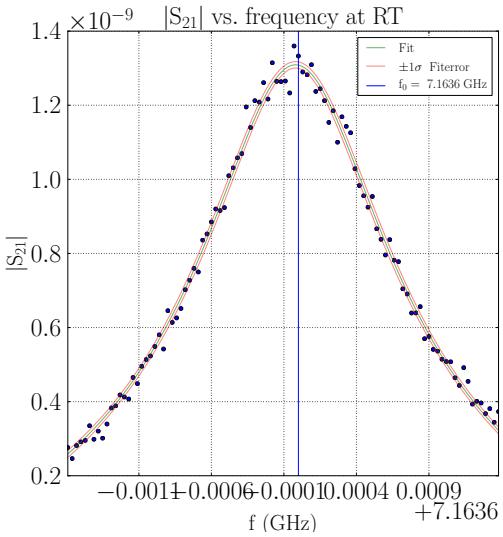

(a) Transmission measurement of the cavity at room temperature. The port length is 2.93 mm. The width of the approximated Lorentzian peak gives an internal quality factor of $Q = 4370$.

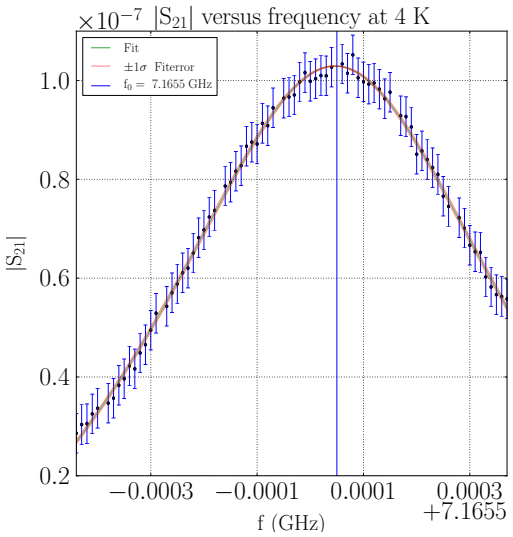

(b) Transmission measurement of the cavity at 4 K. The pin length is 2.93 mm. The width of the Lorentzian peak gives an quality factor of $Q = 10510$.

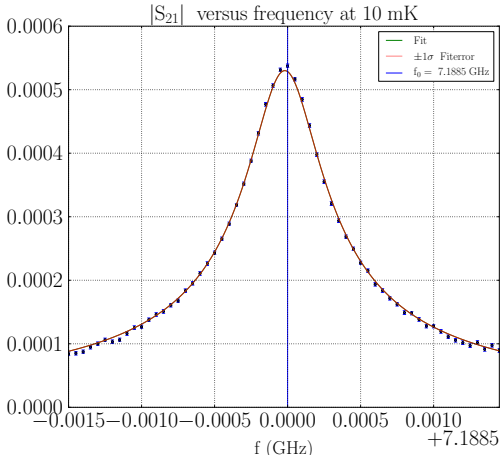

(c) Transmission measurement of the cavity at base temperature. The port length is 3.75 mm. The measurement gives $Q \approx 14700$.

Figure 15: Transmission measurement of the quality factors at room temperature, 4 K and base temperature.

our expectations of the simulated spectroscopy depicted by the dotted graph. We sweep the drive frequency and perform a transmission measurement versus coil current (short lines in the graph) to measure both the tuned qubit frequency and shifted resonant cavity mode. Yellow dots correspond to the cavity frequency and red dots to the qubit system. The full Hamiltonian for Transmon and resonator is used to fit the data.

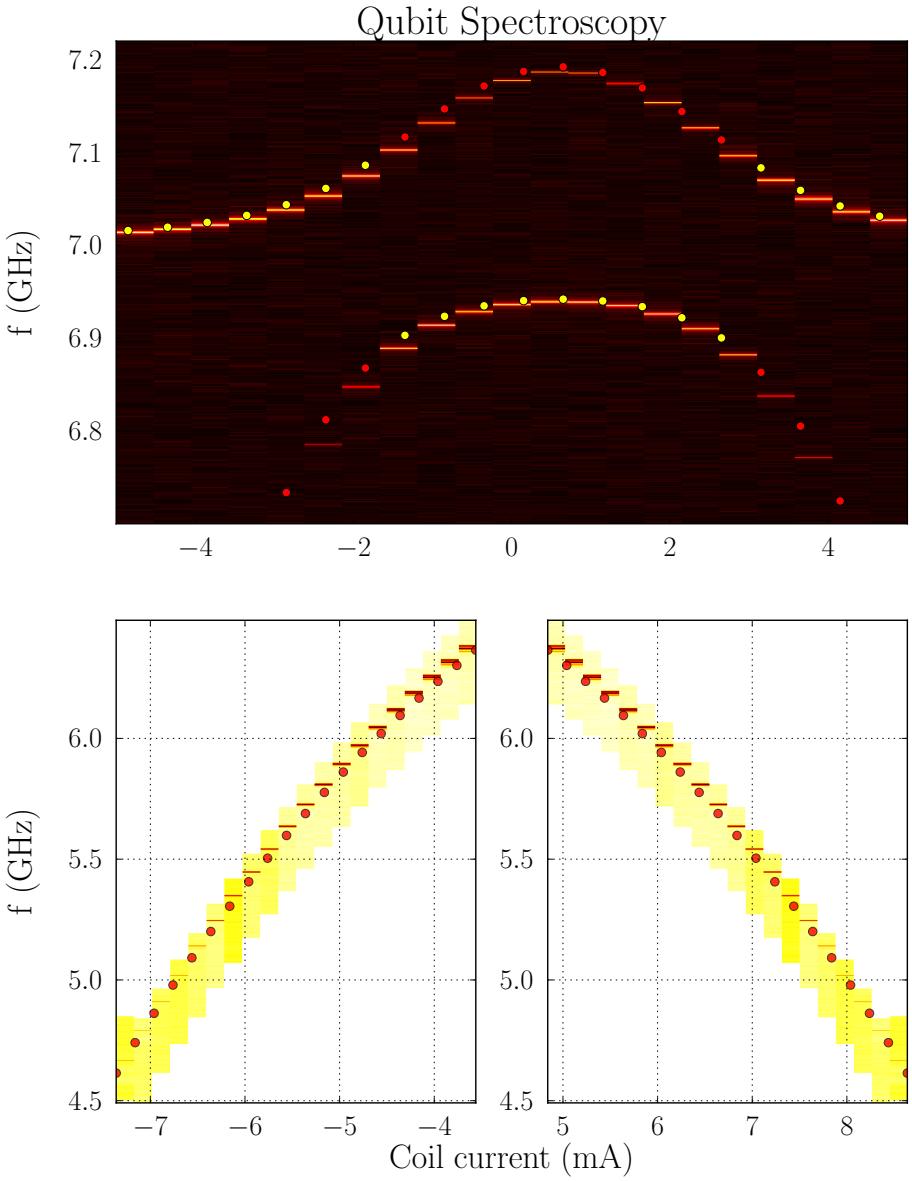

Figure 16: Spectroscopy of the qubit and cavity frequency on the applied B-filed of the external coil. The current range of the coil is big enough to tune the qubit as described in 5.2. The standard coil with $N = 1500$ windings is used. Dots denote the fitted data from the full Hamiltonian of the qubit-resonator system. For the first measurement the coil is supplied with only one voltage source, whereas in the second measurement two sources are used for current values above 5 mA and below −5 mA. Compare also to figure 8 which well agrees to the experimental results. A constant magnetic field from the circulators and the earth's magnetic field result in a slight offset of the whole graph to the right.

7.4 Rabi experiment

A typical feature of a two-level quantum system is the ability to drive Rabi oscillations. The measurement result is depicted in Figure 17 and clearly shows the well known oscillations of the population when applying a resonant pulse, which is then used to calibrate the $\pi-$ and $\frac{\pi}{2}-$pulses for measurement of relaxation and dephasing [5].

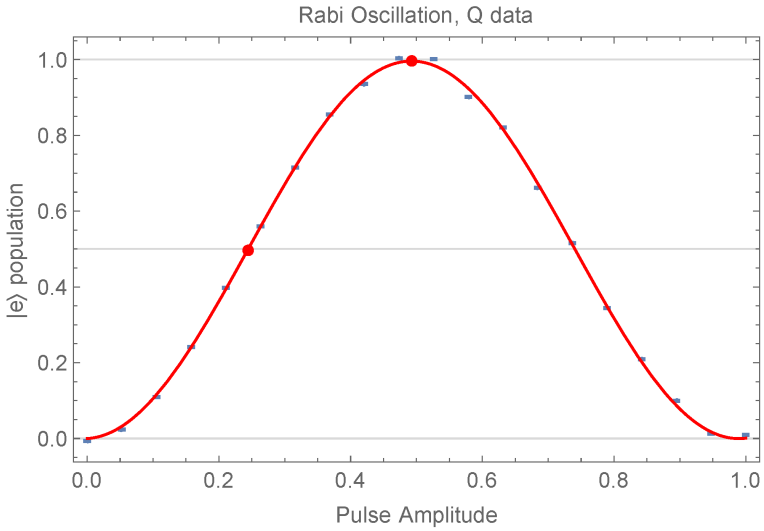

Figure 17: Example of a Rabi oscillation. The visibility of oscillations in population probability proofs the existence of a two-level system.

7.5 Relaxation T_1 and dephasing T_2

7.5.1 T_1 time

The T_1 time is measured by a relaxation experiment as shown in Figure 18. First a $\pi-$pulse is applied to excite the qubit. After the controlled delay Δt the state of the qubit is read out. Averaging over many measurements yields the population probability of the excited state as a function of time. The state of the qubit naturally decays and will eventually end up in the ground state due to vacuum fluctuations or imperfections the qubit can loose its energy to. The time constant of this decay is called relaxation time T_1. In the scenario where all but the fundamental mode of the cavity are far detuned from the qubit transition frequency so that all higher modes can be neglected, a single-mode approximation can be used and the time constant for dispersive decay is given by

$$T_1 = \left(\kappa \frac{g^2}{\Delta^2}\right)^{-1}, \tag{7.3}$$

as described in section 3.2.2, where g denotes the coupling between qubit and cavity mode, Δ the detuning of qubit and resonator, and κ the average photon loss rate.

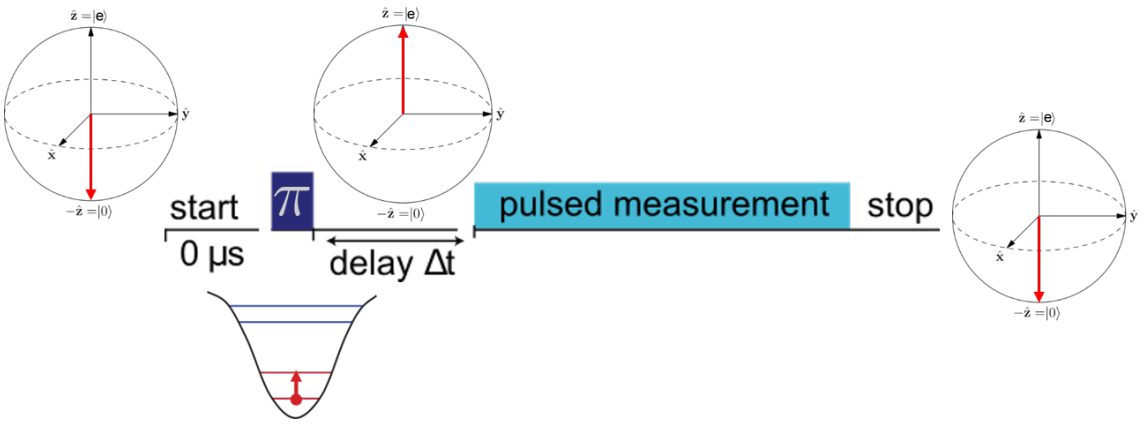

Figure 18: T_1 measurement scheme. The qubit, initially in the ground state, is excited via a $\pi-$pulse. After the delay time parameter Δt a subsequent pulsed measurement of the qubit state follows.

7.5.2 T_2^* time

The measurement of the coherence time of the qubit state during free evolution is obtained by performing a Ramsey experiment. One applies two phase coherent $\frac{\pi}{2}-$pulses which are separated by a delay Δt during which the qubit state processes freely around the $z-$axis. For a given detuning of the drive frequency to the qubit frequency, the $|e\rangle$ state probability displays decaying oscillations of the detuning frequency (see figure 19). The envelope of the oscillations yields the coherence time T_ϕ [1]. The transverse relaxation time is given by

$$T_2^* = \frac{1}{\frac{1}{2T_1} + \frac{1}{T_\phi}}. \tag{7.4}$$

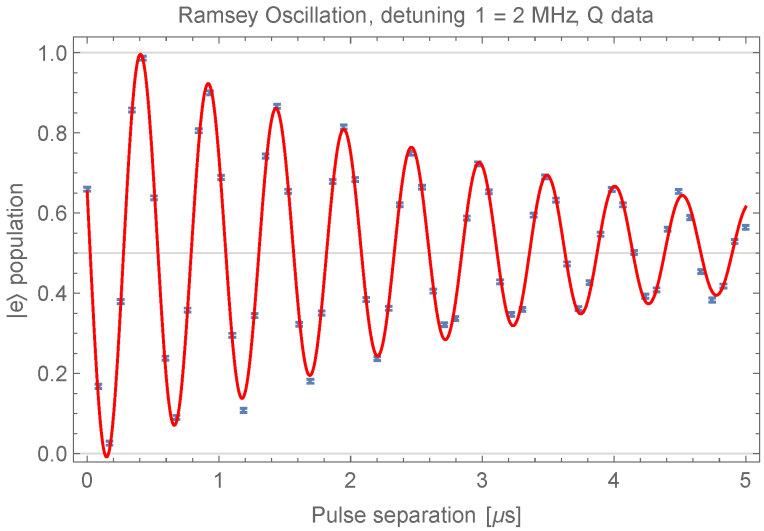

Figure 19: Ramsey experiment to measure the dephasing time T_2^*.

7.5.3 T_2 time

Another way of investigating the dephasing time is a spin-echo measurement. In order to determine the contribution to dephasing of low frequency noise, we perform spin-echo experiments. An intermediate $\pi-$pulse is inserted between the two $\frac{\pi}{2}-$pulses of the Ramsey sequence. The the $\pi-$pulse effectively subtracts the phases accumulated during the two

free evolution time intervals. By symmetry, the total accumulated phase thus is independent of a detuned microwave signal in the cavity. This reveals the decoherence which is not refocused by the intermediate $\pi-$pulse. An exponential decay is measured which we call spin-echo T_2 time [1].

In figure 20 a summary of T_1, Ramsey T_2^* and spin-echo T_2 is depicted as a function of the qubit frequency. The deviation from the Purcell limit in red can be attributed to decay into higher modes, additional flux noise, losses in the sapphire substrate and imperfect superconductivity. However, a fit with an additional decay channel doesn't show consistent results.

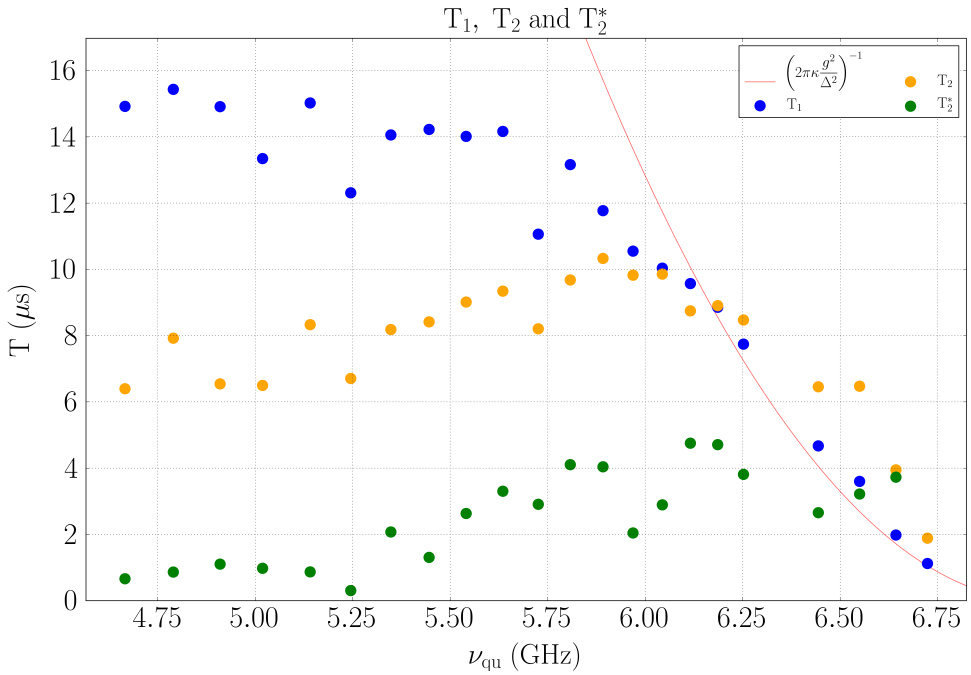

Figure 20: T_1, Ramsey T_2^* and spin-echo T_2 times as a function of the qubit frequency. The Purcell limit in red fits the experimental data only for small deviations from the maximum frequency of the qubit.

8 Conclusion and outlook

In the experiments we achieved tuneability of the transition frequency of the qubit inside a 3D cavity and high T_1 and T_2 times at a relatively low quality factor of the cavity. The results show that a frequency tunable qubit in a 3D cavity has potential in future experiments. Compared to planar resonators, 3D cavities should have less sensitivity to dielectric and conducting losses at surfaces and interfaces. The T_1 relaxation time of the qubit reaches values of $T_1 \approx 15$ µs in a milled copper cavity with no further surface treatment apart from short chemical etching with citric acid. The inner surface quality of the cavity significantly influences the T_1 time for the resulting quality factor determines the average photon loss in the Purcell rate (see equation 7.3). Higher Q values could be achieved with additional treatment like polishing, lapping or chemical processing. The desired tuneability of the qubit makes it necessary to avoid superconducting materials for the cavity since the external field of the coil doesn't pass through the cavity walls at cryogenic temperatures. Nevertheless, superconductivity could still be employed by coating the inside of the cavity with superconducting films, e.g. out of niobium and leaving

out a hole in the film where the coil's B-field can penetrate [2]. This would probably lead to a substantial improvement of the cavity's quality factors.

Appendices

A Transmon design summary

E_C/h	292 MHz
E_J/h	24 GHz
f_0	7.2 GHz
κ	$2\pi \cdot 1.1$ MHz
$g/(2\pi)$	107.7 MHz
SQUID area	49 μm^2
a	300 µm
b	440 µm
c	200 µm
A	7 mm
B	4.3 mm
C	0.44 mm

Table 1: Transmon design and measured SQUID values.

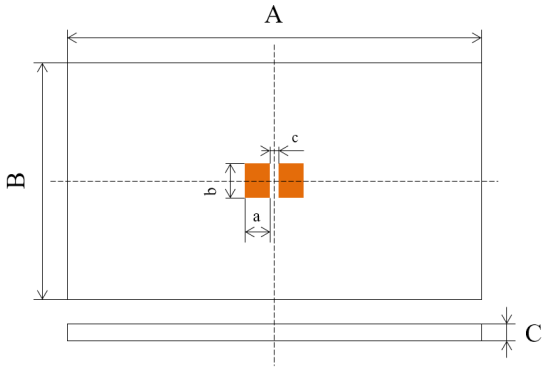

Figure 21: Transmon qubit on a sapphire chip. The chip's dimensions are A, B, C. The orange rectangles depict the capacitor pads of the Transmon qubit.

B Blochsphere

We rewrite the constants in polar coordinates and take out one of the phases

$$|\psi\rangle = e^{i\phi_1}(r_1|0\rangle + r_2 e^{i(\phi_2-\phi_1)}|1\rangle) \tag{B.1}$$

to see that for all $\phi_1 \in [0, 2\pi]$ the probabilities of projecting on the basis states remains the same. The restriction of normalization of the c_i further allows us to write

$$|\psi\rangle = e^{i\phi_1}(\cos(\theta)|0\rangle + \sin(\theta)e^{i\phi}|1\rangle) \tag{B.2}$$

such that $|\psi\rangle$ is fully characterized by ϕ and θ, since we can neglect the arbitrary phase ϕ_1. With this conventions we can represent the state of the quibit as a vector with length 1 on the so called Bloch sphere denoted in figure 22 .

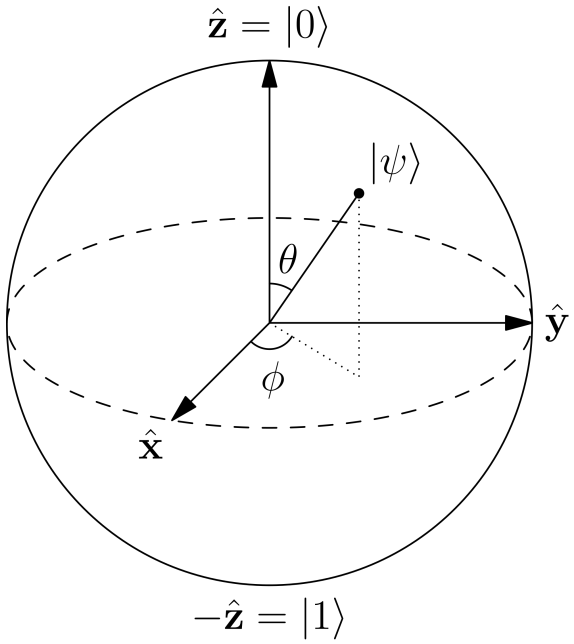

Figure 22: Bloch's representation of the qubit state $|\psi\rangle$ with a vector on the unit sphere characterized by the spherical coordinates ϕ and θ.

C Rabi Oscillations

Let $|0\rangle$, $|1\rangle$ be the solution the solutions to the 2-level system described by H_0 and the Schroedinger equation $H_0|\psi\rangle = E_n|\psi\rangle$. The full Hamiltonian be $H(t) = H_0 + H_1(t)$, where $H_1(t) = \hbar\Omega\cos(\omega t)$ is the time-dependent perturbation of the system. We make an ansatz for the solution of the time dependent Schroedinger equation (TDSE) $H(t)|\psi\rangle = i\hbar\partial_t|\psi\rangle$ as following

$$|\psi(t)\rangle = c_0(t)e^{-iE_0t/\hbar}|0\rangle + c_1(t)e^{-iE_1t/\hbar}|1\rangle \tag{C.1}$$

and find with substituting in the TDSE

$$c_0(t) = \left(\cos\left(\frac{\Omega' t}{2}\right) - i\frac{\Delta}{\Omega}\sin\left(\frac{\Omega' t}{2}\right)\right)e^{i\Delta t/2} \tag{C.2}$$

$$c_1(t) = -i\frac{\Omega}{\Omega'}\sin\left(\frac{\Omega' t}{2}\right)e^{i\Delta t/2}, \tag{C.3}$$

where $\Omega' := \sqrt{\Omega^2 - \Delta^2}$, $\Delta := \omega_{01} - \omega$ and $\omega_{01} := \frac{E_1 - E_0}{\hbar}$. From the solution we see a periodic variation of the occupation probabilities of the two states.

D Electromagnetic modes in 3D cavity

We follow the approach in [7] to derive the electromagnetic modes inside a 3D cavity. With a sineoide ansatz for the time dependence ($e^{-i\omega t}$) the Maxwell equations inside the wave read as

$$\nabla \cdot \vec{E} = 0,\ \nabla \times \vec{E} = i\omega\vec{B} \tag{D.1}$$

$$\nabla \cdot \vec{B} = 0,\ \nabla \times \vec{B} = -i\omega\epsilon_0\mu_0\vec{E} \tag{D.2}$$

The fields fulfill the wave equation

$$\left(\Delta + \frac{\omega^2}{c^2}\right)\begin{pmatrix}\vec{E}\\ \vec{B}\end{pmatrix} = 0 \tag{D.3}$$

A waveguide with constant cross section is translation invariant perpendicular to the cross section (let's say z-axis) and we can therefore work with plane waves

$$\vec{E} = \vec{E}(x,y)e^{\pm ikz - i\omega t} \tag{D.4}$$

$$\vec{B} = \vec{B}(x,y)e^{\pm ikz - i\omega t} \tag{D.5}$$

The wave equation then reduces to a 2D problem

$$(\overbrace{\partial_x^2 + \partial_y^2}^{\Delta_t} + \overbrace{\frac{\omega^2}{c^2} - k^2}^{\gamma^2}) \begin{pmatrix} \vec{E} \\ \vec{B} \end{pmatrix} = 0 \tag{D.6}$$

We separate in longitude and transverse fields

$$\vec{E} = \overbrace{\vec{E}_t}^{(\hat{z}\times\vec{E})\times z} + \overbrace{\vec{E}_z}^{\vec{E}_z \cdot \hat{z}}, \ \vec{B} = \vec{B}_t + \vec{B}_z \tag{D.7}$$

and rewrite the Maxwell equations

$$\pm ik\vec{E}_t + i\omega\hat{z} \times \vec{B}_t = \nabla_t E_z \tag{D.8}$$

$$\pm ik\vec{B}_t - \mu_0\epsilon_0 i\omega\hat{z} \times \vec{E}_t = \nabla_t B_z. \tag{D.9}$$

With D.8, D.9 we can immediately find $\vec{E}_t$ and $\vec{B}_t$ if we know E_z and B_z, since the equations have reduced to a algebraic problem. The continuity conditions on the currentless and chargeless boundary surface S of the waveguide further give us

$$E_z|_S = 0 \tag{D.10}$$

(tangential component of $\vec{E}$ is continuous)

$$\partial_n B_z|_S = 0 \tag{D.11}$$

(normal component of $\vec{B}$ is continuous), where n is the normal vector on S. Our problem eventually reduces to

$$(\Delta_t + \gamma^2) \begin{pmatrix} E_z \\ B_z \end{pmatrix} = 0 \tag{D.12}$$

$$E_z|_S = 0, \ \partial_n B_z|_S = 0. \tag{D.13}$$

For the rectangular waveguide with dimensions (a,b) we find

$$E_{zmn}(x,y) = E_{mn}\sin(m\pi/a)\sin(n\pi/b), \ m,n \in \mathbb{Z}\backslash 0 \tag{D.14}$$

(for TM modes, $E_z|_S = 0$) and

$$B_{zmn}(x,y) = B_{mn}\cos(m\pi/a)\cos(n\pi/b), \ m,n \in \mathbb{Z}, \text{not both } 0 \tag{D.15}$$

(for TE modes $\partial_n B_z|_S = 0$) with

$$\gamma_{mn}^2 = \pi^2\left(\frac{m^2}{a^2} + \frac{n^2}{b^2}\right). \tag{D.16}$$

If we terminate the waveguide on both sides with ideal conductors we get standing waves in z direction

$$A\sin(kz) + B\cos(kz). \tag{D.17}$$

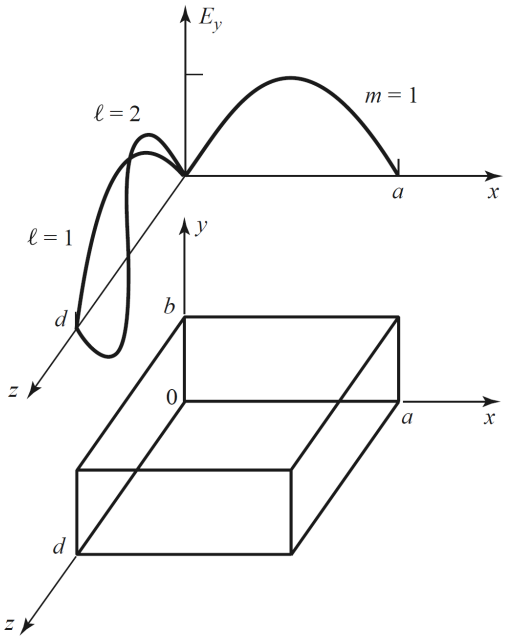

Figure 23: The fundamental modes TE_{101} and TE_{102} in a rectangular cavity. The frequencies in the cavity only can take discrete values.

Placing the walls at $z = 0$, $z = d$ yields

$$E_{z,cavity} = E_z \cos\left(\frac{l\pi z}{d}\right), \; l \in \mathbb{Z} \tag{D.18}$$

(TM modes) and

$$B_{z,cavity} = B_z \sin\left(\frac{l\pi z}{d}\right), \; l \in \mathbb{Z} \tag{D.19}$$

(TE modes). With the z component of the $\vec{E}$ and $\vec{B}$ field we immediately find the transverse fields with D.8 and D.9. The boundary condition in $z = 0$ and $z = d$ fixes the last degree of freedom in $k^2 = \omega^2/c^2 - \gamma^2$ and the eigenfrequencies become discrete

$$\omega_{mnp}^2 = c^2\pi^2 \left(\frac{m^2}{a^2} + \frac{n^2}{b^2} + \frac{l^2}{d^2}\right). \tag{D.20}$$

Figure 23 shows some modes of a rectangular cavity.

References

[1] M. H. Devoret, A. Wallraff, and J. M. Martinis (2004), *Superconducting Qubits: A Short Review*. arXiv:cond-mat/0411174. .

[2] Yarema Reshitnyk, Markus Jerger and Arkady Fedorov (2016), *3D microwave cavity with magnetic flux control and enhanced quality factor*. arXiv:quant-ph:1603.07423v1.

[3] T. D. Ladd, F. Jelezko, R. Laflamme, Y. Nakamura, C. Monroe and J. L. OBrien (2010), *Quantum computers*. doi:10.1038/nature08812.

[4] Susanne Richer (2013), *Perturbative analysis of two-qubit gates on transmon qubits*. Master's thesis, ETH Zurich.

[5] Romeo Alessandro Bianchetti (2010), *Control and readout of a superconducting artificial atom*. Diss. ETH No. 19174.

[6] Jens Koch, Terri M. Yu, Jay Gambetta, A. A. Houck, D. I. Schuster, J. Majer, Alexandre Blais, M. H. Devoret, S. M. Girvin, and R. J. Schoelkopf (2007), *Charge-insensitive qubit design derived from the Cooper pair box*. Physical Review A 76, 042319 (2007).

[7] David M. Pozar (2012), *Microwave Engineering, Fourth Edition*. John Wiley & Sons, Inc., ISBN 978-0-470-63155-3.

[8] *COMSOL Multiphysics Modeling Software*. COMSOL.com. Comsol, Inc. Retrieved 20 November 2015.

[9] *ANSYS Maxwell 15.0*. Retrieved from http://www.ansys.com/Products/Electronics/ANSYS-Maxwell.

[10] *Autodesk Inventor*. Retrieved from http://www.autodesk.in/products/inventor/compare-products.